

See discussions, stats, and author profiles for this publication at: <https://www.researchgate.net/publication/280803017>

# Role of Ion – Ion Correlations on Fast Ion Transport: Molecular Dynamics Simulation of Na<sub>2</sub>Ni<sub>2</sub>TeO<sub>6</sub>

DATASET · AUGUST 2015

---

READS

28

2 AUTHORS, INCLUDING:



Padmanabhan Padma Kumar

Indian Institute of Technology Guwahati

33 PUBLICATIONS 639 CITATIONS

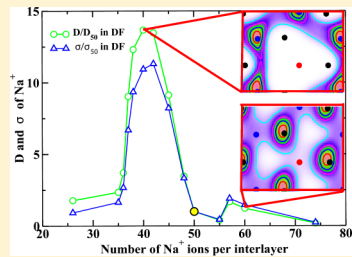
SEE PROFILE

# Role of Ion–Ion Correlations on Fast Ion Transport: Molecular Dynamics Simulation of $\text{Na}_2\text{Ni}_2\text{TeO}_6$

Kartik Sau and P. Padma Kumar\*

Department of Physics, Indian Institute of Technology Guwahati, India

**ABSTRACT:** A series of molecular dynamics (MD) simulations are carried out, in which the  $\text{Na}^+$  content at the interlayers of  $\text{Na}_2\text{Ni}_2\text{TeO}_6$  is systematically varied, keeping the overall charge neutrality of the system, to identify the role of ion–ion correlation on  $\text{Na}^+$  diffusion in the system. It has been observed that interlayers having about 20% lower concentration of  $\text{Na}^+$  facilitate the highest conductivity that is one order of magnitude higher than those having normal  $\text{Na}^+$  concentration. The simulations predict a gradual crossover from energy-driven to entropy-driven transport of  $\text{Na}^+$  ions with the  $\text{Na}^+$  concentration at the interlayers. The transport mechanism and pathways of the mobile ions are also modified.



## INTRODUCTION

The search for better fast ion conductors for battery and fuel cell applications is one of the most active fields in concurrent materials research.<sup>1,2</sup> Development of all-solid-state batteries based on Li has received the most attention for their lightweight and high energy density. Li-ion batteries are the favorite for small scale applications such as powering portable electronic devices, and have been leading the market for over a decade.<sup>3–11</sup> However, Na-based materials are gaining renewed attention owing particularly to their low cost and natural abundance and thus make better candidates for medium and large scale energy storage applications.<sup>12–18</sup>

Theoretical approaches, such as atomistic computer modeling and molecular dynamics (MD) simulations, are widely employed to augment the search for optimal materials for battery and fuel cell applications.<sup>19–27</sup> These techniques have the unique distinction of space–time resolutions at molecular–picosecond levels and are thus capable of providing fresh insights on the ion transport mechanism and factors influencing it.<sup>28–30</sup> Further, simulations permit “virtual experiments” to be performed under conditions experimentally inaccessible or extremely difficult to achieve, for a better understanding of the governing principles of physicochemical processes.<sup>20</sup>

The present MD study follows our recent modeling and MD simulations<sup>31</sup> of  $\text{Na}_2\text{M}_2\text{TeO}_6$  (where M = Ni, Zn, Co, and Mg), focusing on the Ni composition.  $\text{Na}_2\text{Ni}_2\text{TeO}_6$  consists of layers of edge-shared  $\text{NiO}_6$  and  $\text{TeO}_6$  octahedra, forming honeycomb-like ordering on the *ab*-plane (see Figure 1). The  $\text{Na}^+$  ions intercalate face-shared trigonal-prismatic sites at the interlayers, resulting in high 2D conductivity ( $\sigma = 4\text{--}11 \text{ S/m}$ ) at 300 °C.<sup>32,33</sup>

The MD simulations presented here investigate the role of ion–ion interaction in transport properties, by tuning the  $\text{Na}^+$  concentration at the interlayers. It should be noted that the variation of conductivity with mobile ion concentration is universally observed in several fast ion conductors. In fact, it is an integral part of traditional experimental strategy to improve the conductivity by making aliovalent substitution around a

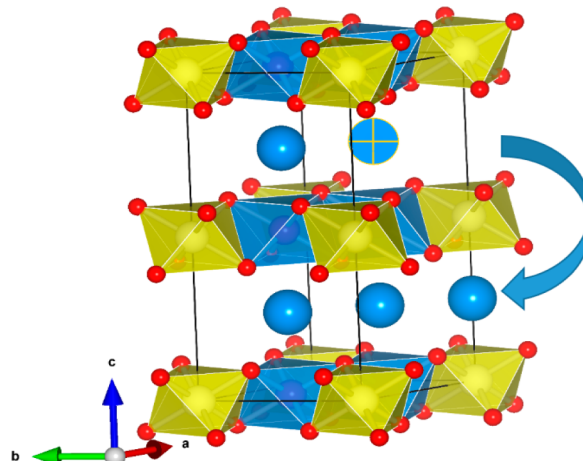


**Figure 1.** Rhombohedral unit cell of the  $\text{Na}_2\text{Ni}_2\text{TeO}_6$  structure having edge-shared octahedral layers parallel to the *ab*-plane;  $\text{NiO}_6$ -octahedra (blue) and  $\text{TeO}_6$ -octahedra (yellow), along with the fringe oxygens (red balls) necessary for completing the octahedra, are shown. The Na atoms (blue balls) are shown transferred between interlayers schematically.

parent composition, once a framework solid with promising ion transport properties is synthesized.<sup>27,34–38</sup> However, such aliovalent substitutions also result in changes in lattice parameters, thereby modifying the geometrical bottlenecks for ion transport. A typical example is the NASICONs,  $\text{Na}_{1+x}\text{Zr}_2\text{Si}_x\text{P}_{3-x}\text{O}_{12}$ , where the highest ionic conductivity is observed around  $x = 2$ , where the *c*-parameter of the rhombohedral lattice, and bottlenecks for ion transport, attains a maximum.<sup>39</sup> Further, aliovalent substitutions modify the Coulombic barriers for ion migration, depending on the ordering of the framework ions.<sup>23,24</sup> Thus, experimental

Received: April 29, 2015

Revised: July 15, 2015



ACS Publications

© XXXX American Chemical Society

A

DOI: 10.1021/acs.jpcc.5b04087  
*J. Phys. Chem. C* XXXX, XXX, XXX–XXX

outcome is in general a combined effect of various factors such as the mobile ion concentration, changes in structural parameters, cationic ordering of the host lattice, etc. The present computational study, by virtue of the minimal structural changes with variation in  $\text{Na}^+$  loading, provides fresh insights on the exclusive role of ion–ion interaction on transport properties.

## METHODOLOGY

MD simulations are performed on  $\text{Na}_2\text{Ni}_2\text{TeO}_6$ , employing the Vashishta–Rahman form of interatomic potential,<sup>23,24</sup>

$$u_{ij}(r_{ij}) = \frac{q_i q_j}{4\pi\epsilon_0 r_{ij}} + \frac{A_{ij}(\sigma_i + \sigma_j)^{n_{ij}}}{r_{ij}^{n_{ij}}} - \frac{P_{ij}}{r_{ij}^4} - \frac{C_{ij}}{r_{ij}^6} \quad (1)$$

where  $q_i$  is the partial charge and  $\sigma_i$  is the ionic radius of the  $i$ th ion. The first term represents the effective Coulombic interaction between ion pairs,  $i$  and  $j$ , separated by a distance  $r_{ij}$ , with  $\epsilon_0$  being the permittivity of the free space.  $A_{ij}$ ,  $P_{ij}$ , and  $C_{ij}$  are respectively the prefactors controlling the overlap–repulsion between electron clouds, interactions due to atomic polarization, and van der Waals attraction between ion pairs  $i$  and  $j$ . Notably, the overlap–repulsion term of the potential is softer in nature, with  $n = 11$ , 9, or 7, respectively, for cation–cation, cation–anion, and anion–anion pairs, compared to Born–Mayer (Buckingham)<sup>40</sup> or Lennard–Jones forms.<sup>34,41–43</sup> An optimized set of parameters for the  $\text{Na}_2\text{M}_2\text{TeO}_6$  family of solids, where  $\text{M} = \text{Ni}, \text{Co}, \text{Zn}$ , or  $\text{Mg}$ , has been reported by us recently.<sup>32</sup> Table 1 reproduces the parameters

**Table 1. Interionic Potential Pair Parameters Employed in Present Study**

ion (X)	$q_X$ (C)	$\sigma_X$ (Å)	$A_{\text{Na}-X}$ (eV)	$A_{X-\text{O}}$ (eV)	$C_{X-\text{O}}$ (eV Å <sup>6</sup> )	$P_{X-\text{O}}$ (eV Å <sup>4</sup> )
$\text{Na}^+$	0.65	1.13	2.298	0.1061	0.00	0.0
$\text{Ni}^{2+}$	1.30	0.69	24.256	3.0846	59.85	31.0
$\text{Te}^{6+}$	3.90	0.70	9.081	3.9098	17.15	11.3
$\text{O}^{2-}$	-1.30	1.21	0.106	0.9260	85.14	0.0

$n_{ij} = 11$ , 9, or 7, respectively, for cation–cation, cation–anion, and anion–anion.

for  $\text{Na}_2\text{Ni}_2\text{TeO}_6$ , which is subsequently employed in the present study. Note that plausible changes in interatomic potential with local  $\text{Na}^+$  concentration is not incorporated due to unavailability of experimental data.

The simulation supercell comprises  $5 \times 5 \times 2$  rhombohedral ( $P\bar{6}_3/mcm$ ) unit cells of  $\text{Na}_2\text{Ni}_2\text{TeO}_6$  containing a total of 1100 ions (200  $\text{Na}^+$ , 200  $\text{Ni}^{2+}$ , 100  $\text{Te}^{6+}$ , and 600  $\text{O}^{2-}$ ). The structure consists of  $\text{TeO}_6$  octahedra-sharing edges with the surrounding  $\text{NiO}_6$  octahedra, in a hexagonal honeycomb order, forming layers parallel to the  $ab$ -plane (see Figure 1). The supercell consists of four interlayers, perpendicular to the  $c$ -axis, each containing 50  $\text{Na}^+$  ions over the  $5 \times 5$  unit cells on the  $ab$ -plane.

As mentioned earlier, the present study focuses on the role of ion–ion correlation in the transport of ions in the solid. In order to effect modifications on the ion–ion interactions, while maintaining the overall charge neutrality of the system, we have varied the concentration of the  $\text{Na}^+$  at the interlayers. Note that overall charge neutrality of the system is an essential condition for the use of Ewald summation that is typically employed in simulations to ensure the convergence of long-range

Coulombic interactions. Thus, starting structures with different numbers of  $\text{Na}^+$ ,  $50 + y/50 - y/50 + y/50 - y$ , where  $y$  is an integer zero to 24 (that is, about 50% of the normal) are prepared; this quartet of numbers represents the number of  $\text{Na}^+$  ions at the four interlayers perpendicular to the  $c$ -axis and in order over the  $5 \times 5$  unit cells on the  $ab$ -plane comprising the simulation supercell. The interlayers having different loadings are analyzed separately, which shall be referred to by the number of  $\text{Na}^+$  ions confined in the interlayer across the  $5 \times 5$  unit cells henceforth.

Starting from the X-ray positions of the framework ions (Ni, Te, and O) and  $\text{Na}^+$  ions distributed randomly across the Na1 and Na2 sites identified in the X-ray studies,<sup>33</sup> a series of MD simulations are carried out in the following ensembles:

(1) Most of the results presented here are based on a series of microcanonical ensemble (NVE) MD simulations, allowing all atoms to move (dynamic framework). These simulations of 12 ns duration (of which the first 6 ns are dedicated to equilibration) are performed at the experimental density. During the first nanosecond of the 6-ns-long equilibration, velocities of atoms are scaled at intervals to achieve a resulting average temperature of 600 K. The resulting (time averaged) temperatures (over the production phase) in all cases of loadings are well within  $\pm 10$  K around the aspired value of 600 K.

(2) Isothermal–isobaric ensemble (NPT) MD simulations allowing for changes in shape and size of the supercell are carried out at 300 K and at 1 atm pressure. The NPT-MD simulations are 6 ns long, at a time step of 2 fs. The objectives of these runs are solely to scrutinize the structural stability and changes in lattice parameters (with respect to the experimental values) upon different loadings of  $\text{Na}^+$  ions at the interlayer of  $\text{Na}_2\text{Ni}_2\text{TeO}_6$ .

(3) A series of NVE-MD simulations are performed with the framework ions (Ni, Te, and O) immobilized (static-framework) at their X-ray positions,<sup>33</sup> allowing only the  $\text{Na}^+$  ions to move. These 12-ns-long runs are performed at a desired temperature of 600 K (with the temperatures controlled by velocity-scaling during first nanosecond of the 6-ns-long equilibration to result in an eventual accuracy of  $\pm 10$  K over the production phase). As discussed in the next section, for extreme loadings, having above  $\pm 30\%$   $\text{Na}^+$  ions at the interlayer, some degree of bending and sliding of layers are noted in NPT- and NVE-MD runs. The objectives of these static-framework runs are to ensure that the qualitative nature of the results are unaffected with respect to these structural imperfections at extreme loadings.

The temperatures mentioned in the rest of the article are the desired values for NVE-MD runs, in static as well as dynamic framework calculations, which include a tolerance value of  $\pm 10$  K. Ewald summation technique and periodic boundary conditions are employed in all cases. The NPT-MD simulations are performed using LAMMPS (employing a tabular form of the potential in eq 1) and NVE-MD simulations, both in the dynamic and static frameworks, using our in-house software.

## RESULTS AND DISCUSSION

**Structure.**  $\text{Na}_2\text{Ni}_2\text{TeO}_6$  forms layers of edge-shared  $\text{NiO}_6$  and  $\text{TeO}_6$  octahedra, arranged in a honeycomb order parallel to the  $ab$ -plane (Figure 1). The interlayers of these metal oxide slabs, having a spacing of about 3.5 Å (measured between oxygen layers), accommodate the charge-balancing  $\text{Na}^+$  ions. Each unit cell consists of two interlayers, each containing two

**Table 2. Comparison of the Lattice Parameters from Experiment (at 300 K),<sup>33</sup> Calculated from NPT-MD at 300 K, and Their Respective Percentage ( $\Delta$ ) Deviations for Systems Having Variably Loaded Interlayers, 50/50/50/50 (50/50), 55/45/55/45 (55/45), and 60/40/60/40 (60/40)**

lattice parameters	experiment	50/50	$ \Delta (\%)$	55/45	$ \Delta (\%)$	60/40	$ \Delta (\%)$
$a$ (Å)	5.207	5.211	0.06	5.226	0.36	5.224	0.30
$b$ (Å)	5.207	5.213	0.10	5.223	0.30	5.224	0.30
$c$ (Å)	11.156	11.163	0.06	11.216	0.53	11.204	0.43
$\alpha$ (degree)	90	90.02	0.02	90.01	0.01	89.96	0.04
$\beta$ (degree)	90	89.97	0.03	91.28	0.30	89.98	0.02
$\gamma$ (degree)	120	120.04	0.03	119.95	0.04	119.99	0.01

$\text{Na}^+$  ions per unit cell. Previous MD simulations have shown that metal oxide layers are impenetrable, leading to anisotropic conduction of  $\text{Na}^+$  in the *ab*-plane.

The present NPT-MD simulations of  $\text{Na}_2\text{Ni}_2\text{TeO}_6$  for the various  $\text{Na}^+$  loadings produced average cell dimensions and angles close to the normally loaded 50/50/50/50-system and within 0.5% of the experimental values. However, for the extreme loadings having  $\pm 30\%$  or more  $\text{Na}^+$  ions (that is 65/35/65/35 composition and beyond), some degree of sliding, and bending or undulations, of the layers is noted. This prompted us to carry out a series of static framework simulations and to eliminate the influence of structural imperfections on the transport properties. Table 2 provides a comparison of the average cell parameters from NPT-MD simulations at 300 K for the 60/40/60/40, 55/45/55/45, and 50/50/50/50 loadings. Thus, the interlayer spacings are practically insensitive to the loading (except for the structural imperfections at extreme loadings mentioned above) and thus are not a significant factor for the observed changes in the  $\text{Na}^+$  diffusivities, to be discussed later. The radial distribution functions forms,  $g(r)$ , between select ion pairs, Ni–O, Te–O, and O–O, for these loadings are shown in Figure 2. The peak positions of these  $g(r)$  compare well with the  $g(r)$  calculated from the X-ray structure (shown as vertical bars) for the corresponding ion pairs. Also, Ni and Te make a sharp oxygen

coordination of six, as expected. Thus, the  $[\text{Ni}_2\text{TeO}_6]^{2-}$ -framework permits a significant degree of compositional variation of  $\text{Na}^+$  at its interlayers.

**Ionic Conductivity.** Having observed that the  $[\text{Ni}_2\text{TeO}_6]^{2-}$ -framework permits up to  $\pm 30\%$  variation in the number of  $\text{Na}^+$  ions at the interlayers without appreciable structural changes, detailed investigation of  $\text{Na}^+$  transport at the interlayers is carried out. For each of the individual interlayers having different  $\text{Na}^+$  loadings, the diffusivity of  $\text{Na}^+$  is calculated from the mean squared displacement (MSD) versus time, using the Einstein relation,

$$D = \lim_{t \rightarrow \infty} \frac{1}{4Nt} \left\langle \sum_{j=1}^N [\vec{r}_j(t) - \vec{r}_j(0)]^2 \right\rangle \quad (2)$$

where  $r_j$  is the position vector of the  $j$ th  $\text{Na}^+$  ion,  $t$  the period of observation, and  $N$  the number of  $\text{Na}^+$  ions in a given interlayer. The angular bracket implies averaging over several time origins. The factor of 4 at the denominator, instead of six, implies an estimated two-dimensional diffusivity, as there is no long-range motion of  $\text{Na}^+$  along the *c*-axis. The mean squared displacement of  $\text{Na}^+$  ions confined to individual interlayers at 600 K is shown in Figure 3 for  $\text{Na}^+$  loadings over the range of 40 to 60. The corresponding dc conductivity is calculated using the Nernst–Einstein relation,

$$\sigma = \frac{Nq^2 D}{V k_B T} \quad (3)$$

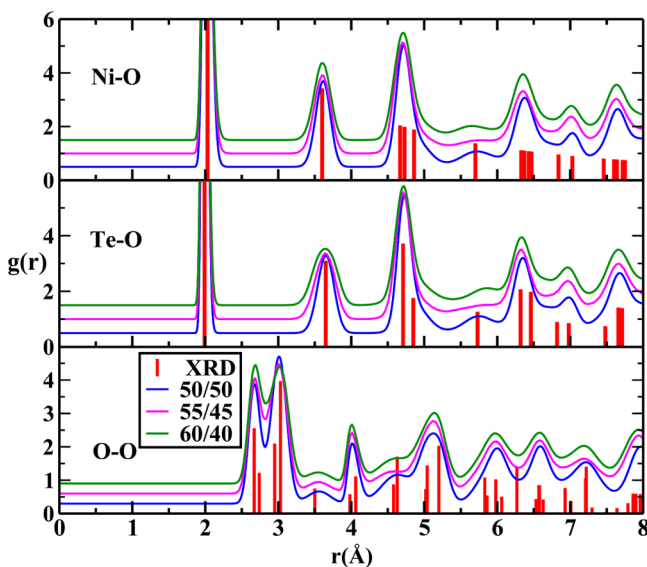


**Figure 2.** Radial distribution function (RDF),  $g(r)$ , between select ion pairs, Ni–O, Te–O, O–O, of  $\text{Na}_2\text{Ni}_2\text{TeO}_6$  for different loadings from NPT-MD simulations at 300 K. The  $g(r)$  values calculated for the X-ray structure<sup>33</sup> are shown as vertical bars in red. The functions are displaced uniformly along the Y-axis for clarity.

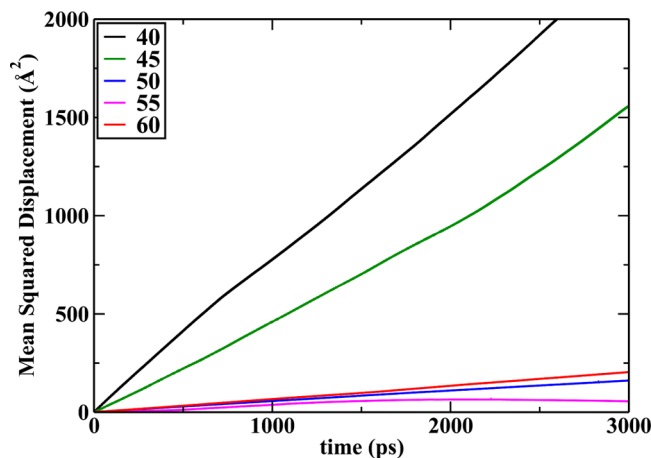


**Figure 3.** Mean square displacement (MSD) of  $\text{Na}^+$  ions for a few interlayers having different loadings of  $\text{Na}^+$  in  $\text{Na}_2\text{Ni}_2\text{TeO}_6$  from NVE-MD (dynamic framework simulations) at 600 K. The legend indicates the number of  $\text{Na}^+$  ions per interlayer across  $5 \times 5$  unit cells on the *ab*-plane.

where  $N$  is the number of  $\text{Na}^+$  ions per unit cell in a given interlayer and  $V$  is half the unit cell volume (as there are two interlayers per unit cell).  $q$  is the formal charge of  $\text{Na}^+$  (+1e),  $k_B$  the Boltzmann constant, and  $T$  the temperature in Kelvin. The diffusion coefficients from dynamic (DF) and static (SF) frameworks, as well as ionic conductivity, at 600 K, all relative to their respective normally loaded interlayer (having 50  $\text{Na}^+$  ions), are shown in Figure 4 as a function of  $\text{Na}^+$  loadings. The

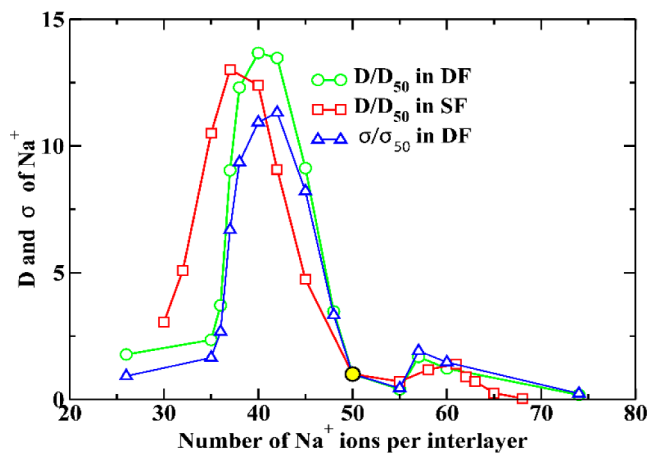


**Figure 4.**  $\text{Na}^+$  diffusion coefficients ( $D$ ) and conductivity ( $\sigma$ ) in the dynamic framework (DF) for variably loaded interlayers are shown relative to their respective values of the normal interlayer (having 50  $\text{Na}^+$  ions, marked by the yellow circle), from NVE-MD simulations at 600 K. The diffusivities in the static (SF) framework relative to its normal interlayer are also shown.

$\text{Na}^+$  diffusivities of the normally loaded interlayer at 600 K are estimated to be 0.014 and 0.044  $\text{\AA}^2/\text{ps}$ , respectively, for the dynamic (DF) and static (SF) frameworks. This, roughly 3-fold, enhancement of  $\text{Na}^+$  diffusivity in the static framework (SF) is fairly uniform across the composition range. A qualitative understanding of this enhancement may be derived, noting that in the static framework the  $\text{Na}^+$  ion recoils off the framework more vigorously than in the dynamic case (this can be argued by drawing the parallel to an elastic, head-on collision of two masses where the recoil velocity of the lighter particle (analogous to  $\text{Na}^+$ ) increases with the mass of the other particle (analogous to the static framework)). This high recoil velocity translates to higher cage-frequency of oscillation of the  $\text{Na}^+$  ions. A higher cage-frequency (attempt-frequency) enhances the diffusivity of the ions.

The  $\text{Na}^+$  diffusivity in the static and dynamic framework, as well as the conductivity (calculated for the dynamic framework), shows remarkably anomalous behavior with peak values around the loading state of 40 (Figure 4). Thus, a reduction in the  $\text{Na}^+$  concentration at the interlayers by about 20% (from the normal loading state of 50) enhances the conductivity through nearly one order of magnitude. The observed trend suggests that further reduction does not favor the  $\text{Na}^+$  transport. Because negligible changes in lattice parameters are observed over  $\pm 30\%$  variation in the number of  $\text{Na}^+$  ions (that is, over 40 to 60  $\text{Na}^+$  loadings) at the interlayers, the observed effect is attributed largely to the changes in ion–ion interaction due to the change in  $\text{Na}^+$  concentration.

**Microscopic  $\text{Na}^+$  Transport.** Three crystallographically different  $\text{Na}^+$  sites, named Na1, Na2, and Na3, are identified in the X-ray studies of Evtigneeva et al.<sup>32</sup> These sites respectively

have multiplicities of three, two, and one at each interlayer per unit cell. All three sites have a trigonal bipyramidal arrangement of oxygens, three from the top and three from the bottom metal oxide layers as shown in Figure 5. For the Na2 site, the three

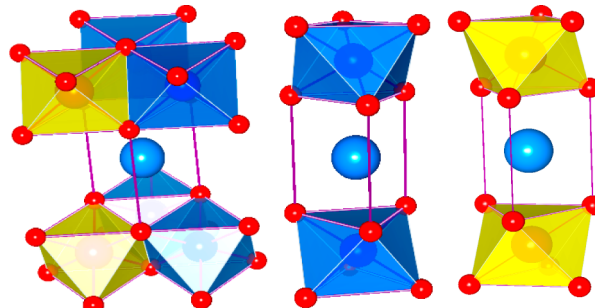


**Figure 5.** Polyhedral environments of the different Na sites, Na1, Na2, and Na3 (from left to right).  $\text{NiO}_6$  octahedra are shown in blue and  $\text{TeO}_6$  octahedra in yellow.

oxygens above and below are the triangular faces of two  $\text{NiO}_6$  octahedra from the top and bottom layers, while for the Na3 site the triangular faces are of  $\text{TeO}_6$  octahedra on top and bottom layers. The Na1 site is aligned along the tetrahedral voids, due to the face sharing of the polyhedra, and has two Ni and one Te neighbor each from top and bottom layers.

The potential energy of individual  $\text{Na}^+$  ions is calculated as,

$$u_i = \sum_{\substack{j=1 \\ j \neq i}}^{N_t} u_{ij} \quad (4)$$

where  $N_t$  is the total number of particles in the system, and  $u_{ij}$  is the interaction potential in eq 1, such that the total potential energy of the system is,

$$u_t = \frac{1}{2} \sum_{i=1}^{N_t} u_i \quad (5)$$

The 6 ns trajectories from NVE-MD simulations at 600 K are analyzed for energetics, site occupancy, and migration pathways of  $\text{Na}^+$ . The potential energy of the individual  $\text{Na}^+$  ions (due to the rest of the ions in the system), averaged over the MD trajectory and over all the  $\text{Na}^+$  ions in a given interlayer, is mapped onto the *ab*-plane. The potential energy surface (PES) thus generated, spanning  $2 \times 2$  unit cells, is shown in Figure 6 for three different  $\text{Na}^+$  loadings, namely, 40, 50, and 60. The right column displays the corresponding population of  $\text{Na}^+$  ions, again mapped over  $2 \times 2$  unit cells on the *ab*-plane. Locations of the  $\text{Na}^+$  sites, Na1, Na2, and Na3, are also marked in the backdrop.

In the underloaded interlayer (having 40  $\text{Na}^+$  ions, that is, 20% lower concentration) a deep potential minimum of about  $-2.76$  eV is observed at the Na2 site, with no appreciable minimum at the Na1 site. The population of  $\text{Na}^+$  ions shown in the top right column also follows the trend, with an estimated 70% of the  $\text{Na}^+$  ions at the Na2 site, leaving the Na1 and Na3 sites practically unvisited. We should note that owing to the presence of the two  $\text{Te}^{6+}$  neighbors at a distance of 2.78 Å, the Na3 site is expected to be of higher energy for an occupying  $\text{Na}^+$  ion and thus least preferred. It turns out that the Na2 site having two  $\text{Ni}^{2+}$  neighbors at a distance of 2.78 Å has the lowest energy among the three. The Na1 site is intermediate in energy

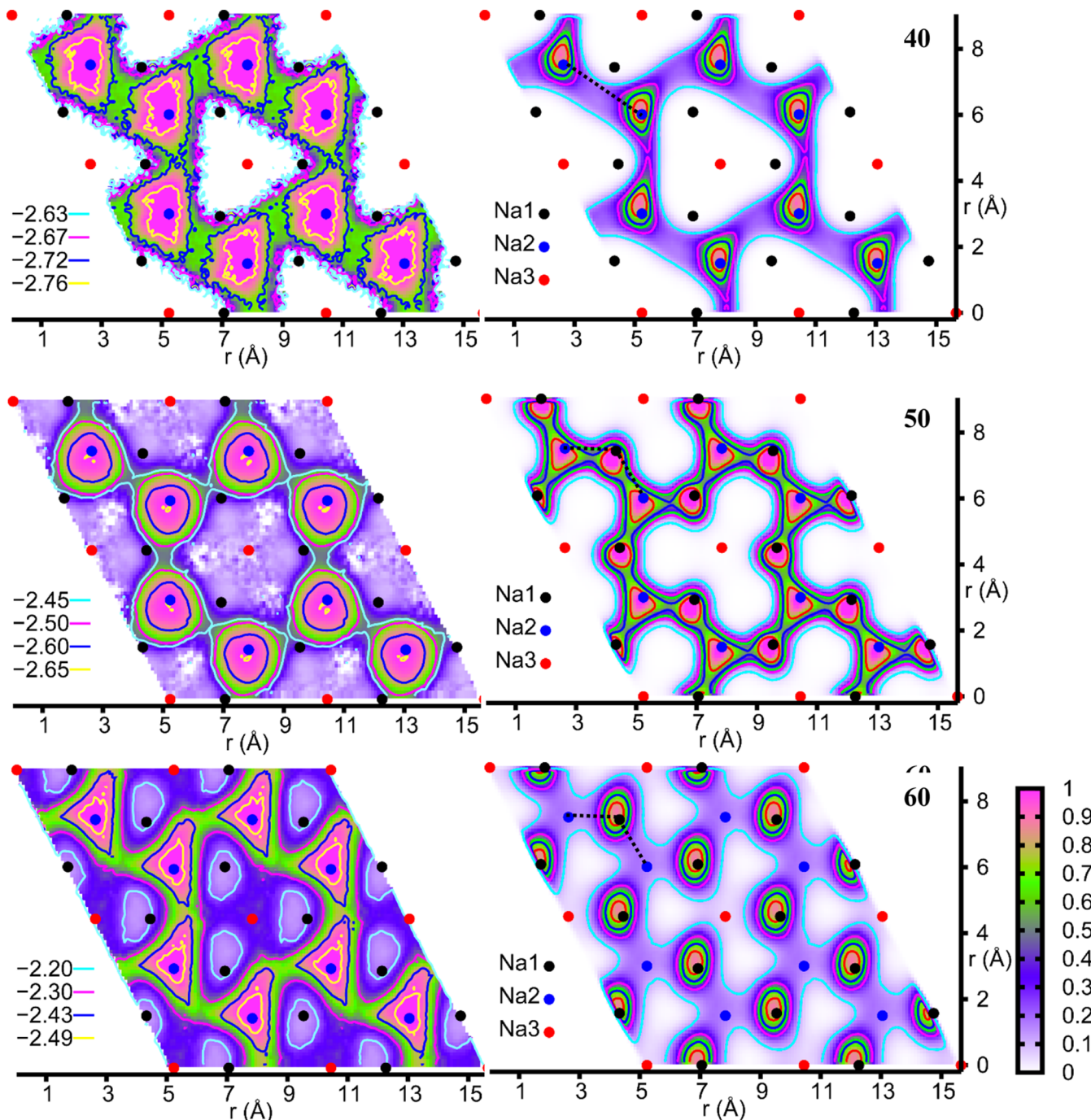


**Figure 6.** From top to bottom, (left-column) the potential energy profile in eV (as in eq 4), and (right-column) population profile of  $\text{Na}^+$  ions from NVE-MD (dynamic framework simulations) at 600 K (mapped onto  $2 \times 2$  unit cells), for the underloaded, normal, and overloaded interlayers, having respectively 40, 50, and 60  $\text{Na}^+$  ions. The population profiles are normalized with respect to their respective peak values, and the color map on the extreme right is common to all loadings. The locations of the Na sites, Na1, Na2, and Na3, from X-ray study are marked by the common legends shown in the middle.

due to its two  $\text{Te}^{6+}$  and four  $\text{Ni}^{2+}$  neighbors but at a larger distance of 3.32 and 3.26 Å, respectively. The migration pathway of  $\text{Na}^+$  ions in this case connects two neighboring Na2 sites directly.

The PES for the normal-loaded interlayer (having 50  $\text{Na}^+$  ions), too, shows a deep minimum at the Na2 sites and hardly any minimum at the Na1 site. But the population profile (middle, right column) depicts a contrasting picture, wherein the Na1 and Na2 sites have nearly matching occupancy. The preferred migration pathway now connects nearby Na1 and

Na2 sites. The overloaded interlayer (having 60  $\text{Na}^+$  ions, of 20% higher concentration) still has the Na2 sites offering the lowest energy, at about  $-2.49$  eV, now higher by 0.27 eV compared to the underloaded case. Interestingly, the population at Na2 is very low at 12%, and Na1 accommodates most  $\text{Na}^+$  ions at a given instant despite being energetically unfavorable. The Na3 sites still remain scarcely visited. The preferred migration channel for the  $\text{Na}^+$  remain Na2–Na1–Na2, though much less traversed in comparison with the normal-loading agreeing with the low conductivity calculated.

For the sake of clarity, the one-dimensional potential energy profiles of the  $\text{Na}^+$  along its migration channels connecting the stretch of a given  $\text{Na}_2$  site to one of its neighboring  $\text{Na}_2$  sites for different loadings are shown in Figure 7. These energies are

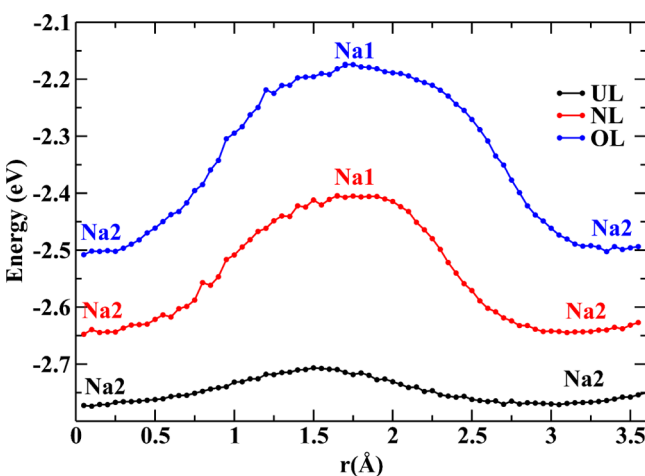


**Figure 7.** Average potential energy barriers (eq 4) for  $\text{Na}^+$  hops from a  $\text{Na}_2$  site to a neighboring  $\text{Na}_2$  site for underloaded (UL), normal-loaded (NL), and overloaded (OL) cases from NVE-MD simulations at 600 K. The potential energies are sampled along the approximate migration path (marked by dotted lines on the population profile shown in the right column of Figure 6) and projected along the line joining the  $\text{Na}_2$  sites.

sampled from the two-dimensional potential energy profiles (left-column, in Figure 6) along the approximate  $\text{Na}^+$  migration paths marked by the dotted line in the two-dimensional population profiles in the right-column of Figure 6. The abscissa is the projected distance of the migration channel to a straight line connecting neighboring  $\text{Na}_2$  sites. Evidently, the average potential energies as well as migration barriers for  $\text{Na}^+$  increase with the loading. The estimated barrier heights are roughly 0.07, 0.24, and 0.33 eV, respectively, for the underloaded (having 40  $\text{Na}^+$  ions), normal (having 50  $\text{Na}^+$  ions), and overloaded (having 60  $\text{Na}^+$  ions).

The above observations can be summarized as follows. In the underloaded interlayer the  $\text{Na}^+$  ions are largely guided by the framework, as the  $\text{Na}^+-\text{Na}^+$  repulsion is marginal owing to low concentration. The populations and pathways of  $\text{Na}^+$  migration are dictated solely by the potential energy landscape. In the normal-loaded interlayer the  $\text{Na}^+-\text{Na}^+$  interactions are more significant, and their average energies are higher (more toward the positive). The ions now start exploring higher energy regions of the landscape in an effort to avoid each other and populate energetically less favorable sites ( $\text{Na}_1$ ). As noted in our previous study,  $\text{Na}^+$  ions maintain a distance of more than 2.5 Å (see Figure 8), which holds for all the loadings examined presently as well. This forbids simultaneous occupation of neighboring  $\text{Na}_1$  and  $\text{Na}_2$  sites (which are only about 1.67 Å away). Populating the higher energy sites increases the entropy of the system, owing to the additional configurations now accessible, or in other words creates greater disorder. As detailed in our earlier study, as the numbers of  $\text{Na}_2$  sites and  $\text{Na}^+$  ions are equal in the normal-loaded interlayer (two in an interlayer per unit cell), a disordered  $\text{Na}^+$  sublattice is imperative for their transport in this system. Upon further loadings (60 loading corresponds to 2.4  $\text{Na}^+$ /unit cell/interlayer), the  $\text{Na}^+$  ions, now in excess of the comfortable

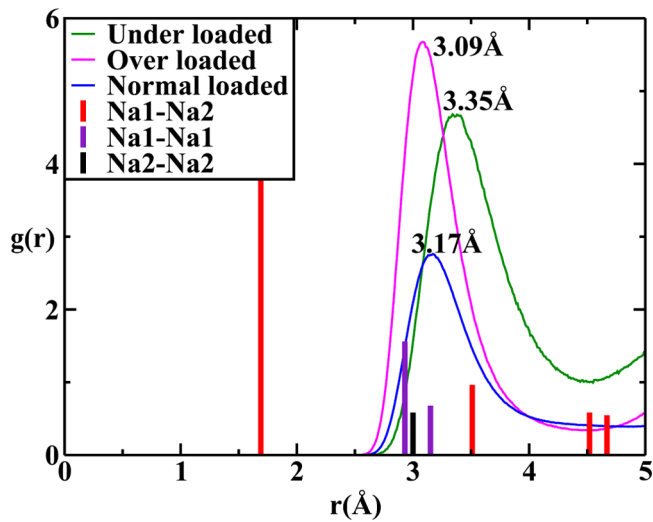


**Figure 8.** Radial distribution functions,  $g(r)$ , for pair  $\text{Na}-\text{Na}$  for three interlayers such as underloaded, overloaded, and normal loaded in  $\text{Na}_2\text{Ni}_2\text{TeO}_6$  from NVE-MD (dynamic framework simulations) at 600 K.  $\text{Na}_1-\text{Na}_1$ ,  $\text{Na}_1-\text{Na}_2$ , and  $\text{Na}_2-\text{Na}_2$  for the X-ray structure<sup>33</sup> are shown as vertical bars.

$\text{Na}_2$  sites (2  $\text{Na}^+$ /unit cell/interlayer), opt for  $\text{Na}_1$  sites that are higher in number (3  $\text{Na}^+$ /unit cell/interlayer). In fact, any appreciable occupancy at  $\text{Na}_2$  is unfavorable, as this brings them closer to one or more  $\text{Na}^+$  ions occupying neighboring  $\text{Na}_1$  sites. Thus, with the increase in concentration of mobile ions, ion-ion repulsions turn out to be an important factor in controlling the site occupancies and migration path of ions. Consequently, ion transport is dictated more and more by the entropic factors rather than energetic considerations.

**Hop Mechanism.** The mechanism and time scales of ion hops in the lattice can be deduced from the self-part of the van Hove correlation function  $G_s(r,t)$ , given by,

$$G_s(r,t) = \frac{1}{N} \sum_{i=1}^N \langle \delta(r - |r_i(t) - r_i(0)|) \rangle \quad (6)$$

where  $N$  is, in general, the number of  $\text{Na}^+$  ions in the system (in the present case the number of  $\text{Na}^+$  ions in a particular interlayer),  $r_i(t)$  refers to the position of the ion after a delay time  $t$ , and  $\delta$  is the Dirac delta function.  $G_s(r,t)$  describes the probability distribution that an ion initially at the origin  $t = 0$  is found at a distance  $r$  after a time  $t$ . Figure 9 shows the  $\text{Na}^+$  distributions for the underloaded (40  $\text{Na}^+$  ions/interlayer/simulation supercell), normal, and overloaded cases. In the underloaded case (left-panel) the  $G_s(r,t)$  at a delay time of 1 ps suggests the distribution just at the onset of developing the second peak. At a delay time of 20 ps, a the fully developed second peak around 3.14 Å, corresponding to the nearest neighbor distance of two  $\text{Na}_2$  sites, is evidenced. The distribution shifts to larger distances with considerable spread at longer times as the  $\text{Na}^+$  ions diffuse away from the original site.

For the normal-loaded case (50  $\text{Na}^+$  ions/interlayer/simulation-supercell) shown in the middle panel of Figure 9, the residence time of the  $\text{Na}^+$  ions is larger and the second peak starts developing around 20 ps consistent with its one order lower diffusivity compared to the underloaded case. In this particular case the emergence of a peak at around 1.67 Å signifies  $\text{Na}^+$  hops between neighboring  $\text{Na}_1-\text{Na}_2$  sites, also by

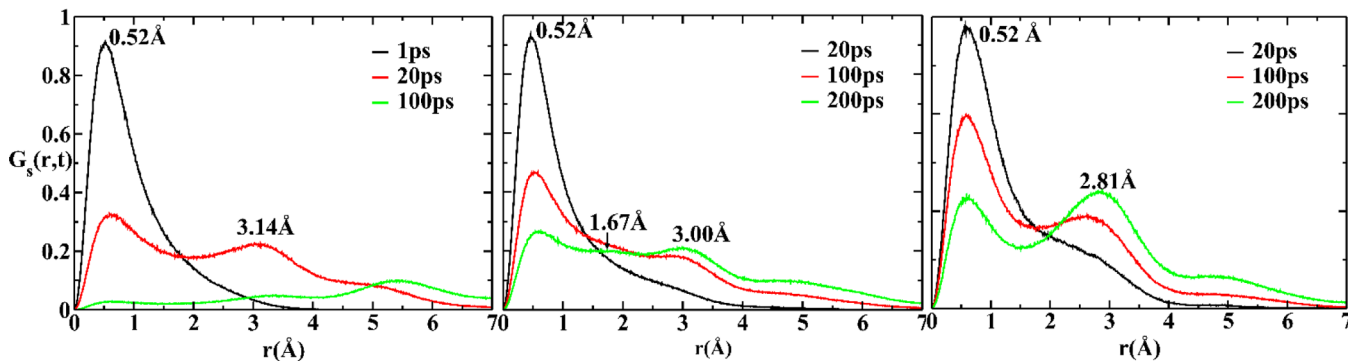


**Figure 9.** Self-part of van Hove correlation function of  $\text{Na}^+$  ions for the three representative cases: underloaded (left), normal (middle), and overloaded (right) interlayers are shown (from dynamics framework NVE-MD at 600 K).

virtue of their comparable population. In the overloaded case (60  $\text{Na}^+$  ions/interlayer/simulation-supercell) the time scales of  $\text{Na}^+$  hops are similar to the normal-loaded interlayer consistent with their comparable  $\text{Na}^+$  diffusivity. The distinction, however, is the absence of the peak around 1.67 Å. Though  $\text{Na}_1\text{--Na}_2\text{--Na}_1$  forms the preferred migration channel in this case, the absence of the peak and the low population of  $\text{Na}_2$  sites suggest that  $\text{Na}^+$  ions make only a brief stopover at the  $\text{Na}_2$  sites before proceeding to the next  $\text{Na}_1$  sites.

## CONCLUSION

The role of ion–ion correlation in  $\text{Na}^+$  transport for  $\text{Na}_2\text{Ni}_2\text{TeO}_6$  is examined, employing molecular dynamics simulation. The  $\text{Na}^+$  diffusivity and conductivity are found to vary by well over one order of magnitude, depending on the  $\text{Na}^+$  content at the interlayers of  $\text{Na}_2\text{Ni}_2\text{TeO}_6$ . It is observed that 20% lower concentration of  $\text{Na}^+$  in the system is optimal to maximize the ionic conductivity in the system. This is almost entirely attributed to ion–ion correlations, as the present study, by design, is devoid of other contributing factors such as lattice expansion and Coulombic barriers due to aliovalent substitution in the framework.

The  $\text{Na}_2$  sites located between two  $\text{NiO}_6$  octahedra on top and bottom metal–oxygen layers are found to be of lowest energy across a range of  $\pm 20\%$  around the standard  $\text{Na}^+$  composition. At low concentrations of mobile  $\text{Na}^+$  ions at the interlayer, the populations follow the energetic comfort of the framework and migration channels involve direct transfer between lowest energy  $\text{Na}_2$  sites. With the increase in concentration of  $\text{Na}^+$ ,  $\text{Na}_1$  sites that are energetically less favorable start populating, and the migration channels connecting  $\text{Na}_2\text{--Na}_1\text{--Na}_2$  emerge. The gradual evolution of the  $\text{Na}^+$  population in favor of sites that are energetically less favorable but higher in multiplicity, and emergence of newer migration channels, reflects on a paradigm shift of energy-driven to entropy-driven mechanism with  $\text{Na}^+$  concentration. This has implication for understanding of transport mechanisms in fast ion conducting solids.

## AUTHOR INFORMATION

### Corresponding Author

\*Phone: +91-3612582718. E-mail: padmakumarp@iitg.ernet.in.

### Notes

The authors declare no competing financial interest.

## ACKNOWLEDGMENTS

The authors acknowledge financial support (grant no.: SR/S1/PC-24/2011) from Department of Science and Technology, New Delhi.

## REFERENCES

- Ivanov-Shitz, A. Computer simulation of superionic conductors: II. Cationic conductors. Review. *Crystallogr. Rep.* **2007**, *52*, 302–315.
- Quararone, E.; Mustarelli, P. Electrolytes for solid-state lithium rechargeable batteries: Recent advances and perspectives. *Chem. Soc. Rev.* **2011**, *40*, 2525–2540.
- Goodenough, J. B. Rechargeable batteries: Challenges old and new. *J. Solid State Electrochem.* **2012**, *16*, 2019–2029.
- Sahu, G.; Lin, Z.; Li, J.; Liu, Z.; Dudney, N.; Liang, C. Air-stable, high-conduction solid electrolytes of arsenic-substituted  $\text{Li}_4\text{SnS}_4$ . *Energy Environ. Sci.* **2014**, *7*, 1053–1058.
- Takada, K. Progress and prospective of solid-state lithium batteries. *Acta Mater.* **2013**, *61*, 759–770.
- Masquelier, C. Solid electrolytes: Lithium ions on the fast track. *Nat. Mater.* **2011**, *10*, 649–650.
- Bron, P.; Johansson, S.; Zick, K.; Schmedt auf der Günne, J. r.; Dehnen, S.; Roling, B.  $\text{Li}_{10}\text{SnP}_2\text{S}_{12}$ : An affordable lithium superionic conductor. *J. Am. Chem. Soc.* **2013**, *135*, 15694–15697.
- Kamaya, N.; Homma, K.; Yamakawa, Y.; Hirayama, M.; Kanno, R.; Yonemura, M.; Kamiyama, T.; Kato, Y.; Hama, S.; Kawamoto, K.; Mitsui, A. A lithium superionic conductor. *Nat. Mater.* **2011**, *10*, 682–686.
- Adams, S.; Rao, R. P. Structural requirements for fast lithium ion migration in  $\text{Li}_{10}\text{GeP}_2\text{S}_{12}$ . *J. Mater. Chem.* **2012**, *22*, 7687–7691.
- Cao, C.; Li, Z.-B.; Wang, X.-L.; Zhao, X.-B.; Han, W.-Q. Recent advances in inorganic solid electrolytes for lithium batteries. *Front. Energy Res.* **2014**, *2*, 25.
- Barghamadi, M.; Best, A. S.; Bhatt, A. I.; Hollenkamp, A. F.; Musameh, M.; Rees, R. J.; Ruther, T. Lithium-sulfur batteries—the solution is in the electrolyte, but is the electrolyte a solution? *Energy Environ. Sci.* **2014**, *7*, 3902–3920.
- Hong, S. Y.; Kim, Y.; Park, Y.; Choi, A.; Choi, N.-S.; Lee, K. T. Charge carriers in rechargeable batteries: Na ions vs. Li ions. *Energy Environ. Sci.* **2013**, *6*, 2067–2081.
- Palomares, V.; Serras, P.; Villaluenga, I.; Hueso, K. B.; Carretero-Gonzalez, J.; Rojo, T. Na-ion batteries, recent advances and present challenges to become low cost energy storage systems. *Energy Environ. Sci.* **2012**, *5*, 5884–5901.
- Hayashi, A.; Noi, K.; Sakuda, A.; Tatsumisago, M. Superionic glass-ceramic electrolytes for room-temperature rechargeable sodium batteries. *Nat. Commun.* **2012**, *3*, 856.
- Ellis, B. L.; Nazar, L. F. Sodium and sodium-ion energy storage batteries. *Curr. Opin. Solid State Mater. Sci.* **2012**, *16*, 168–177.
- Hueso, K. B.; Armand, M.; Rojo, T. High temperature sodium batteries: Status, challenges and future trends. *Energy Environ. Sci.* **2013**, *6*, 734–749.

- (17) Slater, M. D.; Kim, D.; Lee, E.; Johnson, C. S. Sodium-Ion Batteries. *Adv. Funct. Mater.* **2013**, *23*, 947–958.
- (18) Fergus, J. W. Ion transport in sodium ion conducting solid electrolytes. *Solid State Ionics* **2012**, *227*, 102–112.
- (19) Mo, Y.; Ong, S. P.; Ceder, G. First principles study of the  $\text{Li}_{10}\text{GeP}_2\text{S}_{12}$  lithium super ionic conductor material. *Chem. Mater.* **2012**, *24*, 15–17.
- (20) Meller, J. a. Molecular Dynamics. In *eLS*; John Wiley & Sons, Ltd: New York, 2001.
- (21) Hull, S. Superionics: crystal structures and conduction processes. *Rep. Prog. Phys.* **2004**, *67*, 1233–1314.
- (22) Islam, M. S.; Fisher, C. A. Lithium and sodium battery cathode materials: computational insights into voltage, diffusion and nanostructural properties. *Chem. Soc. Rev.* **2014**, *43*, 185–204.
- (23) Vashishta, P.; Rahman, A. Ionic motion in  $\alpha$ -AgI. *Phys. Rev. Lett.* **1978**, *40*, 1337–1340.
- (24) Vashishta, P.; Kalia, R. K.; Rino, J. P.; Ebbsjö, I. Interaction potential for  $\text{SiO}_2$ : A molecular-dynamics study of structural correlations. *Phys. Rev. B: Condens. Matter Mater. Phys.* **1990**, *41*, 12197–12209.
- (25) Walker, J.; Catlow, C. Structure and transport in non-stoichiometric  $\beta$ - $\text{Al}_2\text{O}_3$ . *J. Phys. C: Solid State Phys.* **1982**, *15*, 6151.
- (26) Malavasi, L.; Fisher, C. A.; Islam, M. S. Oxide-ion and proton conducting electrolyte materials for clean energy applications: structural and mechanistic features. *Chem. Soc. Rev.* **2010**, *39*, 4370–4387.
- (27) Razmkhah, M.; Mosavian, M. H.; Moosavi, F.  $\text{Nd}_{2-x}\text{Gd}_x\text{Zr}_2\text{O}_7$  electrolytes: Thermal expansion and effect of temperature and dopant concentration on ionic conductivity of oxygen. *Int. J. Hydrogen Energy* **2014**, *39*, 8437–8448.
- (28) Kamishima, O.; Kawamura, K.; Hattori, T.; Kawamura, J. Origin of activation energy in a superionic conductor. *J. Phys.: Condens. Matter* **2011**, *23*, 225404–225414.
- (29) Roy, S.; Kumar, P. P. Influence of Si/P ordering on  $\text{Na}^+$  transport in NASICONs. *Phys. Chem. Chem. Phys.* **2013**, *15*, 4965–4969.
- (30) Roy, S.; Kumar, P. P. Influence of cationic ordering on ion transport in NASICONs: Molecular dynamics study. *Solid State Ionics* **2013**, *253*, 217–222.
- (31) Sau, K.; Kumar, P. P. Ion transport in  $\text{Na}_2\text{M}_2\text{TeO}_6$ : insights from molecular dynamics simulation. *J. Phys. Chem. C* **2015**, *119*, 1651–1658.
- (32) Evstigneeva, M. A.; Nalbandyan, V. B.; Petrenko, A. A.; Medvedev, B. S.; Kataev, A. A. A new family of fast sodium ion conductors:  $\text{Na}_2\text{M}_2\text{TeO}_6$  ( $\text{M} = \text{Ni, Co, Zn, Mg}$ ). *Chem. Mater.* **2011**, *23*, 1174–1181.
- (33) Berthelot, R.; Schmidt, W.; Sleight, A. W.; Subramanian, M. A. Studies on solid solutions based on layered honeycomb-ordered phases P2- $\text{Na}_2\text{M}_2\text{TeO}_6$  ( $\text{M} = \text{Co, Ni, Zn}$ ). *J. Solid State Chem.* **2012**, *196*, 225–231.
- (34) Ivanov-Schitz, A.; Savvin, S.; Mazo, G. Cationic transport mechanism in  $\alpha$ - $\text{Ag}_{1-x}\text{Cu}_x\text{I}$  ( $0 < x < 0.25$ ): Molecular-dynamics simulation. *Crystallogr. Rep.* **2009**, *54*, 292–298.
- (35) Arbi, K.; Hoelzel, M.; Kuhn, A.; García-Alvarado, F.; Sanz, J. Structural factors that enhance lithium mobility in fast-ion  $\text{Li}_{1+x}\text{Ti}_{2-x}\text{Al}_x(\text{PO}_4)_3$  ( $0 \leq x \leq 0.4$ ) conductors investigated by neutron diffraction in the temperature range 100–500 K. *Inorg. Chem.* **2013**, *52*, 9290–9296.
- (36) Arbi, K.; Rojo, J.; Sanz, J. Lithium mobility in titanium based nasicon  $\text{Li}_{1+x}\text{Ti}_{2-x}\text{Al}_x(\text{PO}_4)_3$  and  $\text{LiTi}_{2-x}\text{Zr}_x(\text{PO}_4)_3$  materials followed by NMR and impedance spectroscopy. *J. Eur. Ceram. Soc.* **2007**, *27*, 4215–4218.
- (37) Saranya, K.; Deviannapoorani, C.; Dhivya, L.; Ramakumar, S.; Janani, N.; Murugan, R.  $\text{Li}_{7-x}\text{La}_3\text{Sn}_{2-x}\text{Nb}_x\text{O}_{12}$  ( $x = 0.25–1$ ) cubic lithium garnet. *Mater. Lett.* **2012**, *77*, 57–59.
- (38) Hafskjold, B.; Li, X. Molecular dynamics simulations of the  $\text{Mg}^{2+}$ -stabilized  $\text{Na}^+$ -beta"-alumina. *J. Phys.: Condens. Matter* **1995**, *7*, 2949–2968.
- (39) Kumar, P. P.; Yashonath, S. Structure, conductivity, and ionic motion in  $\text{Na}_{1+x}\text{Zr}_2\text{Si}_x\text{P}_{3-x}\text{O}_{12}$ : A simulation study. *J. Phys. Chem. B* **2002**, *106*, 7081–7089.
- (40) Lewis, G.; Catlow, C. Potential models for ionic oxides. *J. Phys. C: Solid State Phys.* **1985**, *18*, 1149.
- (41) Parrinello, M.; Rahman, A.; Vashishta, P. Structural transitions in superionic conductors. *Phys. Rev. Lett.* **1983**, *50*, 1073–1076.
- (42) Nomura, K.-i.; Yokoyama, Y.; Kobayashi, M. Particle correlation in  $\alpha$ -AgI. *Solid State Ionics* **2002**, *154–155*, 285–289.
- (43) Boolchand, P.; Bresser, W. Mobile silver ions and glass formation in solid electrolytes. *Nature* **2001**, *410*, 1070–1073.